DEVELOPMENT AND APPLICATION OF A NEW AIR POLLUTION MODELING SYSTEM — PART III. AEROSOL-PHASE SIMULATIONS

MARK Z. JACOBSON

Department of Civil Engineering, Stanford University, Stanford, CA 94305-4020, U.S.A.

Abstract—Result from a new air pollution model were tested against data from the Southern California Air Quality Study (SCAQS) period of 26–29 August 1987. Gross errors for sulfate. sodium, light absorption. temperatures, surface solar radiation, sulfur dioxide gas, formaldehyde gas, and ozone were lowest among parameters compared (1–40%). Gross errors for elemental carbon, organic carbon, total particulate mass, ammonium, ammonia gas. nitric acid gas, and light scattering, were larger (40–61%). Gross errors for particulate nitrate were largest (65–70%). Reducing the baseline land-based particulate emissions inventory to one-third its original value did not affect gross errors significantly; however, it did turn overpredictions into underpredictions for many species. Doubling emissions increased gross errors for nearly all parameters. Setting lateral boundary inflow concentrations of particles to zero caused slight (< 1%) erosion of results for most species. large erosion (10%) for sodium and chloride, but slight improvement (< 1%) for a few species. Setting both lateral inflow and initial concentrations for gases and particles to zero caused severe degradation of results for many species but relatively mild degradation or improvement for a few. Spinning up the meterological model 24 h in advance caused most gross errors to increase. Finally, the presence of aerosols reduced peak daytime surface solar radiation by approximately 6.4% (55 W m^{-2}), increased nighttime temperatures by about 0.77 K, decreased daytime temperatures by about 0.08 K, and increased overall temperatures (day plus night) by 0.43 K compared to a no-aerosol case. The presence of aerosols also caused ozone mixing ratios to decrease by 2%. Copyright © 1996 Elsevier Science Ltd

Key word index: Air quality model. aerosol model, urban temperatures, ozone, Eulerian grid model.

1. INTRODUCTION

In this paper, model results of aerosol and gas pollution buildup in the Los Angeles basin are compared to data. In addition, sensitivity tests are run, and model prediction are used to estimate the effects of aerosols on surface air temperatures and ozone mixing ratios. The model used is GATOR/MMTD. GATOR is a *G*as *A*erosol, *T*ransport, and *R*adiation air quality model (Jacobson, 1994; Jacobson *et al.*, 1996a) while the MMTD is a *M*esoscale *M*eteorological and *T*racer *D*ispersion model (Lu and Turco, 1995; Lu *et al.*, 1996). In an accompanying paper, aerosol processes in the model are described (Jacobson, 1996). Here, simulations of aerosol and gas buildup, together, with feedback, to radiation and meteorology, are carried out.

2. SETUP OF MODEL SIMULATIONS

Predictions from the GATOR/MMTD model were compared to Southern California Air Quality Study (SCAQS) data for 27–28 August 1987. In the following sections, model grids, model variables, ambient data, emission data, initial conditions, boundary conditions, and error checks are discussed.

2.1. Model grids

For simulations over the Los Angeles Basin, the southwest corner of the MMTD model was placed at 33.06°N latitude and 119.1°W longitude, and the dimension was set to 55 west–east grid cells by 38 south–north cells. Each edge of GATOR was placed two grid cells within each edge of MMTD in order to reduce the effects of boundary wind values calculated by MMTD. Thus, GATOR consisted of 51 east–west cells by 34 north–south cells, with a southwest corner at 33.15°N latitude and 119.9°W longitude. Both models used spherical horizontal coordinates with grid spacing of 0.05 degrees west–east (about 4.6 km) and 0.045° south–north (about 5.0 km). Finer horizontal grid resolution can be used; however, because MMTD is a hydrostatic model, smaller grid resolution increases the probability of prediction errors, especially for vertical velocity.

In the vertical, 20 sigma-pressure coordinate layers were used for MMTD while 14 were used for GATOR. The bottom eight layers in both models were the same; however, each of the next six GATOR

layers contained two MMTD layers. The top in both models was set to 250 mb, and the eight lowest layers in both models were set to below approximately 850 mb (about 1.5 km). In sum, the MMTD solved equations in 41,800 grid cells while GATOR solved equations in 24,276 cells.

2.2. Model variables

In MMTD, several variables, including horizontal and vertical wind velocity, vertical turbulent fluxes, air pressure, air temperature, relative humidity, and liquid water content were predicted in each grid cell during each 6-s meteorological time step. In GATOR, 106 gases, 16 aerosol size bins, and 73 constituents per size bin were carried around. Consequently, GATOR required $24,276 \times (16 \times 73 + 106)$ = 30.9 million words (megawords) of computer memory to store species concentrations. Transport in GATOR was split from other calculations every 300 s while chemistry integration and aerosol microphysics and chemistry calculations were split every 900 s to reduce computational time.

The gases, gas-phase chemical reactions, and aerosol species are listed elsewhere (Jacobson, 1994, 1996; Jacobson et al., 1996a). The aerosol species included 18 solids, 24 liquids, and 30 ions, and one category of residual material. The 16 size bins used ranged in 0.014–74 μm in diameter. Initialization of aerosol concentrations in each size bin is discussed in Section 2.5.

2.3. Ambient data for comparison

27–28 August 1987 was simulated because the number of available SCAQS ambient measurements for that period was large (e.g. Lawson, 1990). Also, a detailed California Air Resources Board (CARB) emissions inventory was prepared for that period. One data set used was the SCAQS modeling archive (King et al., 1990), provided by the CARB (B. Croes, personal communication). The archive contains surface mixing ratios of ambient ozone, carbon monoxide, nitrogen dioxide, nitric oxide, sulfur dioxide, non-methane hydrocarbons (NMHCs), and methane, measured at 56 monitoring sites during the period 26–30 August 1987. The archive also contains surface data for temperature, dew point, relative humidity, sea level pressure, wind speed, wind direction, visibility, solar radiation, and other parameters. At least one variable was measured at each of 98 sites.

In addition, SCAQS Sampler data, provided by the CARB (B. Croes, personal communication) were used for comparison. Fitz et al. (1989) developed the Sampler, and Eldering et al. (1994) describe the measurements taken from it during the SCAQS period. Sampler data consisted primarily of aerosol, aerosol precursor, and particle absorption coefficient measurements. The aerosol-phase species measured included elemental carbon, organic carbon, sodium, chloride, ammonium, nitrate, sulfate, and total aerosol mass. The gas-phase species measured included ammonia,

nitric acid, and sulfur dioxide. Aerosol components from the Sampler were divided into sub-2.5 μm and sub-10 μm size regimes. Error limits for sampler data were included in the data set. Reported measurement uncertainties were typically between 4 and 20%; however uncertainties exceeded 40% for some measurements.

In addition, size-resolved aerosol data from John et al. (1989) were used. Such data included 0.05–0.4 μm, 0.4–2.0 μm, and 2.0–15 μm measurements of sodium, chloride, sulfate, nitrate, ammonium at Claremont, Riverside, and Long Beach City College. Other data used for comparison were measurements of formaldehyde (Winer et al., 1989) and particle scattering coefficients (measured by U. Illinois, General Motors, and the SCAQMD, Eldering et al., 1994).

2.4. Emissions

The aerosol and gas emissions inventories used were prepared by the CARB and designated for Wednesday, 26 August through Friday, 28 August 1987 (Allen and Wagner, 1992). The emissions grid extended over a region 325 km east–west by 180 km north–south, with the southeast corner at 33°8'35"N latitude − 119°24'44"E longitude and a resolution of 5 km in each direction.

The speciated and size-resolved particulate emission rates, accumulated over a day, are listed in Table 1. The four size regimes tabulated include < 1 μm, 1–2.5 μm, 2.5–10 μm, and > 10 μm in diameter. The accuracy of the particulate emissions inventory is very uncertain. To estimate the effects of this uncertainty, two sensitivity simulations were run. These are described in Section 3.2, 3.3 and 4.

Of the 42 aerosol substances included in the CARB emissions inventory, 15 were incorporated into species carried in the model. All others were lumped together and emitted in the model as a species called residual. The 15 inventory substances used were elemental carbon, organic carbon, silicon, aluminum, iron, calcium, potassium, manganese, lead, sodium, ammonium, sulfate, chloride, nitrate, and carbonate. These species were emitted into the model as elemental carbon (EC), organic carbon (OC), $SiO_2(s)$, $Al_2O_3(s)$, $Fe_2O_3(s)$, $CaO(s)$, $K_2O(s)$, $Mn_2O_7(s)$, $Pb_2O(s)$, Na^+, NH_4^+, SO_4^{2-}, Cl^-, NO_3^-, and HCO_3^-, respectively. To account for the oxygen in the above species, an appropriate amount of oxygen mass was removed from the other category in the emissions inventory.

While the CARB inventory accounted for four size categories, the model simulated 16 size categories, crossing all four CARB categories. Two steps were taken to distribute inventory mass to model size bins. First, the mass from each CARB size category was distributed to those model bins whose diameters fell within the boundaries of the particular CARB category. In the case of the three largest CARB size categories, the mass was spread evenly among all size

Table 1. Baseline emissions inventory totals (kg d^{-1}) for aerosol componentss as a function of aerosols size

| Substance | Particle size | | | | | |
	$< 1 \mu m$	$1-2.5 \mu m$	$2.5-10 \mu m$	$> 10 \mu m$	All sizes	Total (%)
Other	147,884	86,431	380,221	712,049	326,585	53.167
Silicon	37,312	37,086	183,641	166,527	424,566	17.015
Organic carbon	28,462	9,363	69,991	58,111	165,903	6.649
Aluminum	14,550	14,644	67,991	58,216	155,401	6.228
Iron	7090	7189	37,210	38,947	90,436	3.624
Calcium	5587	5511	32,619	34,028	77,745	3.116
Sulfates	45,922	894	3998	3122	53,936	2.162
Potassium	7364	3586	16,266	18,989	46,205	1.852
Elemen. carbon	28,467	1095	7247	7429	44,238	1.773
Unknown	9919	6745	11,110	11,903	39,677	1.590
Chloride	11,318	814	4535	4796	21,463	0.860
Titanium	1048	877	4241	4716	10,882	0.436
Sulfur	618	573	3216	2129	6356	0.262
Carbonate ion	306	162	2514	1879	4861	0.195
Sodium	569	233	2080	1916	4798	0.192
Manganese	899	521	1511	1824	4755	0.191
Phosphorous	130	286	1660	1148	3224	0.129
Nitrates	1237	147	935	782	3101	0.124
Zinc	226	154	729	674	1783	0.071
Lead	173	156	758	653	1740	0.070
Barium	79	88	544	856	1567	0.063
Ammonium	841	51	120	136	1148	0.046
Strontium	25	42	308	364	739	0.030
Vanadium	94	66	274	280	714	0.029
Copper	132	60	203	208	603	0.024
Cobalt	127	52	158	212	549	0.022
Nickel	130	48	132	158	468	0.019
Chromium	87	26	158	176	447	0.018
Rubidium	11	12	91	100	214	0.009
Zirconium	6	10	80	110	206	0.008
Lanthanum	26	7	52	65	150	0.006
Bromine	68	5	30	24	127	0.005
Arsenic	26	3	10	19	58	0.002
Cadium	9	2	23	16	50	0.002
Antimony	5	3	15	23	46	0.002
Yttrium	2	3	17	22	44	0.002
Tin	6	7	15	14	42	0.002
Indium	5	1	11	12	29	0.001
Mercury	2	1	11	13	27	0.001
Molybdeum	3	1	7	9	20	< 0.001
Silver	5	2	6	6	19	< 0.001
Palladium	3	1	5	10	19	< 0.001
Selenium	3	0	1	2	6	< 0.001
Gallium	0	0	5	0	5	< 0.001
Total	350,776	176,958	834,725	1,132,637	2,495,132	100.00
% of total	14.06	7.09	33.45	45.40	100.0	

Note. The *all sizes* column is a sum over the four columns to its left. Aerosol data were obtained from tapes provided by Allen and Wagner (1993). Component *other* identifies oxygen, hydrogen, and additional components not included in the aerosol analysis. For example, oxygen atoms in oxides of silicons, aluminium, and iron are included as *other*.

bins in the category. In the case of the smallest CARB category (particles $< 1 \mu m$ in diameter), mass was spread using a lognormal distribution. For example, lognormal parameters for automobile emissions of elemental carbon were obtained from data given in Venkataraman and Friedlander (1994).

The CARB emissions inventory includes land-based source only. However, sea spray is an important source of particulate emissions for the Los Angeles basin. Sea spray forms both when wind and waves force air bubbles to burst at the sea surface (Woodcock, 1953) and when wind tears off wave crests to mechanically produce spume droplets (Monahan et al., 1986). Several sea spray and spume drop parameterizations are available in the literature (e.g. Monahan et al., 1983, 1986; Andreas, 1992; Wu, 1993). These models give emissions as a function of wind speed and drop radius. Here, a parameterization

was derived from Monahan et al. (1983) for particle radii between 0.3 and 17 μm. This parameterization was based on measurements of sea spray between 6 and 14 m in altitude above the surface. In addition, the equations of Wu (1992) were used to obtain emissions of spume drops greater than 37.5 μm in radius. Emission rates for particles between 17 and 37.5 μm in radius were interpolated. Wu (1993) has shown that his spume-drop model and the models of Andreas (1992) and Monahan et al. (1986) differed significantly from each other (e.g. Fig. 5 of Wu, 1992) and suggested that the correct spume-drop parameterization has yet to be determined.

Sea spray initially contains all the substances of sea water. Some of the most abundant elements include sodium (1.08 × 10^4 mg ℓ^{-1}), chloride (1.94 × 10^4 mg ℓ^{-1}), magnesium (1.29 × 10^3 mg ℓ^{-1}), sulfur (9.05 × 10^2 mg ℓ^{-1}), calcium (4.12 × 10^2 mg ℓ^{-1}), potassium (3.99 × 10^2 mg ℓ^{-1}), and carbon (2.8 × 10^1 mg ℓ^{-1}) (Lide, 1993). In the model, the species corresponding to each of these elements were assumed initially to be Na$^+$, Cl$^-$, Mg^{2+}, SO$_4^{2-}$, Ca^{2+}, K$^+$, and HCO$_3^-$, respectively. All remaining sea spray mass was assumed to be liquid water.

A summary of the gas-phase emissions inventory used is given in Jacobson et al. (1996a). In addition, an ammonia gas inventory (Russell and Cass, 1986; Gharib and Cass, 1984; Cass et al., 1982) was used. This gridded and hour-dependent inventory contains ammonia emissions for a day in 1982 August; however, the unperturbed inventory was used for 1987 conditions. The overall ammonia emissions rate in this inventory was 164.3 tons per day, with 51.6% of the emission originating from livestock sources, 14.2% originating from domestic sources, 14.5% originating from livestock sources, 14.2% originating from domestic sources, 14.5% originating from soil, and the rest originating from miscellaneous sources (Russell and Cass, 1986). Most emitted ammonia in the inventory originated from the east side of the basin.

2.5. Initial conditions

Initial vertical and horizontal profiles of temperature, dew point (water vapor content), and pressure were interpolated from 12 SCAQS sounding sites in the outside the basin (King et al., 1990) for the early morning of 27 August 1987. Further, sea surface temperatures were interpolated each hour from SCAQS buoy data. However, wind velocities in the model were initialized to zero to ensure mass conservation and to avoid startup waves near mountain regions. The pressure gradients from the initial interpolated pressure field forced winds to generate. The Coriolis force, pressure gradient force, surface drag, and turbulent fluxes affected the equations of motion over time. Diabatic heating and heat advection influenced changes in potential temperature, which affected pressure gradients.

The method of initializing gas-phase mixing ratios was the same as that discussed in Jacobson et al. (1996a). However, in this study, initial mixing ratios were interpolated from observations of 27 August instead of 26 August. Aerosol concentrations were initialized with either zero, background, or interpolated values. During the SCAQS period of 27–30 August 1987, SCAQS Sampler measurements of elemental carbon, organic carbon, ammonium, nitrate, sulfate, sodium, and chloride aerosol concentrations were taken in four-hour intervals at nine sites throughout the basin (Anaheim, Azusa, Burbank, Los Angeles, Claremont, Hawthorne, Long Beach City College, Rubidoux, and San Nicholas Island). The San Nicholas Island (SNI) site lies under relatively clean ocean air, south of Santa Barbara. To initialize background aerosol concentrations, aerosol mass from SNI (data for midnight—5:00 a.m., 27 August 1987) was first distributed among model size bins in one nucleation mode, two sub-accumulation modes, and one coarse particle mode, with a four-modal lognormal distribution. Mass data for the species listed above were available for two size regimes, below 2.5 μm and below 10 μm diameter. For SNI, the difference between the sub-10 μm and sub-2.5 μm mode mass was distributed into the coarse mode. Table 2 shows the mass concentrations at the SNI site for 4:30 a.m., 27 August.

Further, sub-2.5 μm mass was partitioned between the nuclei and two sub-accumulation modes using a marine surface particle nuclei to accumulation mode

Table 2. Observed mass concentrations of several particulate components in two size regimes at SNI at 04:30, 27 August 1987

Species	Mass in particles < 2.5 μm diameter (μg m^{-3})	Mass in particles 2.5–10 μm diameter (μg m^{-3})
Elemental carbon	0.09	0.11
Organic carbon	0.94	0.41
Ammonium	0.8	0.3
Nitrate	0.43	0.97
Sulfate	2.11	0.53
Sodium	—	2.25*
Chloride	0.03	0.81

Note. Data from SCAQS sample.
*Indicates that this value was an average of day and night values at SNI.

volume ratio (0.005:0.995) calculated from Whitby (1978). Since this ratio is similar to his ratio for clean continental nuclei mode particles (0.004:0.996), the marine ratio was used for both continental and marine background distributions.

After the mass of each SCAQS sampler species (EC, OC, SO_4^{2-}, NO_3^-, NH_4^+, Na^+, Cl^-) was estimated for each lognormal mode at San Nicholas Island, the mass was partitioned into model size bins. All other species concentrations, except for that of $H_2O(aq)$, were initialized to zero because of the greater uncertainty in their values.

Subsequently, the values from SNI were distributed horizontally in each grid cell and scaled vertically. The vertical scaling was exponential and forced initial aerosol concentrations to approach 1/20th their surface value at about 850 mb. Next, aerosol species concentrations from the rest of the SCAQS sampler stations were interpolated within a 15 km radius of influence for each stations, using a $1/distance^2$ interpolation dependence. These masses were spread with a four-modal distributions as well, and the lognormal parameters (geometric means diameters and standard deviations) used for forming these distributions were the same as those used to initialize the distribution for Claremont, as described in Jacobson (1996). Finally, the interpolated concentrations were scaled, with pressure, to the top of the morning inversion layer.

To obtain the initial water content in each aerosol size bin throughout the spatial grid, equilibrium calculations were performed on each bin. During the calculations, water content was determined with a water equation, as described in Jacobson et al. (1996b). Determining the initial liquid water content was important for estimating the initial particle number concentration. In sum, initial model aerosol concentration within the basin and over the ocean resembled SCAQS sampler data for the morning of 27 August 1987.

2.6. Boundary conditions

The variable horizontal inflow boundary conditions for gases and meteorological parameters were described in Jacobson et al. (1996a). For aerosols, inflow concentrations were assumed to be the same as the initial background concentrations at the center of each edge of each layer of the model domain. The aerosol concentrations used for inflow were assumed to be constant over time. A sensitivity test was run to test the effect of zero-inflow concentrations. Results are discussed in Section 4.

Inflow concentrations of aerosols at the model top (about 250 mb/10.3 km) were assumed to be zero. Because the period of simulation (2 d) was short and because emissions and gas-to-particle conversion dominated aerosol concentrations, the vertical boundary conditions for aerosols appeared to be a reasonable choice in comparison to other possible ad hoc boundary conditions.

2.7. Error checks

To determine model performance, error checks were performed. These included checks for mean absolute normalized gross error and normalized bias (Tesche, 1988; DaMassa et al., 1992). While actual station data were used to determine observed values for error checks, bilinear interpolation of four surrounding grid cell centers was used to determine model variable values at the stations.

3. MODEL RESULTS

Here, results from a base-case simulation, which included aerosol processes, are compared of SCAQS data. In addition, a simulation was run without the inclusion of aerosols to estimate the effects of aerosols on temperatures and ozone mixing ratios. Finally, five sensitivity simulations were carried out.

All simulations were run for 04:30 PST, 27 August–0:30 PST, 29 August 1987. Table 3 shows statistical results and Figs 1–91 show time-series comparisons of model results to data for the base-case simulation. The figures represent, in most cases, the best results from the base-case simulation. However, for many parameters (e.g. total mass, elemental carbon, organic carbon, sulfate, sodium, formaldehyde, surface solar radiation, light scattering, and light absorption) between 40–100% of all available figures are shown; thus, both above- and below-average results are depicted. The statistics include gross error and normalized bias for several parameters at two specific times and for the entire simulation. The statistics for the entire period indicate that gross errors for sulfate, sodium, light absorption, surface solar radiation, temperature, relative humidity, sulfur dioxide gas, formaldehyde, and ozone were the lowest among the parameters compared. Gross errors for elemental carbon, organic carbon, total mass, ammonium, nitric acid gas, and light scattering were larger, but often relatively low at 14:30 on both days and at several individual locations. Gross errors for nitrate and ammonia gas were largest. Each parameter is discussed in turn.

3.1. Total mass

The first parameter compared is total mass. Total mass was measured with gravimetric techniques at a relative humidity of about 45%. Total mass consisted to the sum of all particle components in the ambient atmosphere, however, the primary difference between ambient and measured total mass was that the liquid water was nearly absent in the latter case. In order to crudely compare model mass at the ambient relative humidity to observed mass at 45% humidity, liquid water was removed from total model mass. The removal of the model liquid water content was justified on the basis that the liquid water content of

Table 3. Gross errors and normalized biases at 14:30 PST, 27 and 28 August and averaged over the entire 44-h model simulatiion, for several aerosol, gas, meterological, and radiative parameters

Parameter	14:30 27 August			14:30 28 August			44-h average		
	No. of comparisons	Gross error (%)	Bias (%)	No. of comparisons	Gross error (%)	Bias (%)	No. of comparisons	Gross error (%)	Bias (%)
$Mass_{10}$	8	31.4	− 31.2	8	26.5	− 19.4	360	50.1	9.3
$Mass_{2.5}$	7	30.2	− 30.2	8	31.6	− 30.8	356	43.9	− 8.1
EC_{10}	8	23.3	− 0.79	8	32.9	9.2	356	50.6	16.2
$EC_{2.5}$	8	19.9	13.3	8	39.0	23.3	356	57.5	29.9
OC_{10}	8	45.1	− 45.1	8	36.9	− 32.7	352	45.4	0.33
$OC_{2.5}$	8	53.3	− 53.3	8	62.5	− 62.5	352	49.0	− 44.1
Na_{10}	8	20.4	− 15.6	8	42.1	− 42.1	360	36.0	− 30.2
NH_{10}^4	8	45.4	40.2	7	24.6	− 11.4	325	45.7	− 0.15
$NH_{2.5}^2$	7	54.1	− 54.1	7	60.8	− 47.2	321	55.2	− 52.3
SO_{10}^2	8	26.0	0.24	8	23.0	− 22.5	360	26.3	− 8.3
$SO_{2.5}^4$	8	36.9	14.7	8	19.3	− 13.2	360	28.4	3.7
NO_{10}^3	8	26.8	14.0	8	57.8	42.7	360	69.8	18.4
$NO_{2.5}^3$	8	55.6	− 55.6	8	49.0	− 27.7	360	67.8	− 20.7
Cl_{10}	1	22.7	22.7	1	57.9	57.9	190	46.8	16.0
$O_3(g)$	34	20.9	− 12.2	32	23.9	− 8.7	571	27.8	− 6.6
$SO_2(g)$	8	39.5	− 39.5	10	42.0	− 13.0	339	35.4	− 24.2
$NH_3(g)$	7	45.4	− 13.8	6	78.5	32.9	269	69.3	− 25.6
$NHO_3(g)$	7	22.9	20.6	6	53.8	31.8	109	54.6	22.3
$HCHO(g)$	2	17.9	17.9	2	32.8	32.8	61	45.8	32.9
Temp.	14	0.61	0.29	14	0.92	0.59	628	0.63	0.09
Rel. hum.	8	16.4	13.5	8	12.6	− 4.8	358	21.6	4.2
Solar rad.	2	4.3	− 4.3	2	6.3	− 6.3	50	7.9	− 3.0
σ_{sp}	2	37.8	− 30.1	2	22.9	− 22.9	125	43.0	− 13.8
σ_{ap}	6	22.4	16.5	5	49.3	49.3	255	3.98	16.3

Note. The subscripts (10) and (2.5) indicate the mass of the species that resides in particles $< 10 \,\mu m$ or $< 2.5 \,\mu m$ in diameter, respectively. Mass is total particle mass, EC is elemental carbon, OC is organic carbon, solar rad is the sum of surface solar radiation $(W \, m^{-2})$ at $< 5 \,\mu m$ wavelength, σ_{sp} is the extinction coefficient due to scattering by particles, and σ_{ap} is the extinction coefficient due to absorption by particles. Cutoff mixing ratios were 50 ppbv for $O_3(g)$, 5 ppbv for $SO_2(g)$, 5 ppbv for $HCHO(g)$, 1 ppbv for $NH_3(g)$, and 3 ppbv for $HNO_3(g)$. Additional cutoff values were $0.5 \,\mu g \, m^{-3}$ for sub-10 μm chloride, $2.0 \,\mu g \, m^{-3}$ for sub-2.5 μm ammonium, $0.02 \, km^{-1}$ for σ_{ap}, $10 \, W m^{-2}$ for solar radiation, and 0 for all other parameters.
* Indicates the comparison was made or 13:30 27 August since datum was unavailable for 14:30.

aerosols at 45% relative humidity is typically $< 10 \,\mu g \, m^{-3}$ and frequently $< 2 \,\mu g \, m^{-3}$, based on equilibrium calculations (e.g. Pilinis *et al.*, 1987, 1989) while total non-water mass usually ranges from 50 to $150 \,\mu g \, m^{-3}$.

Table 3 shows that normalized gross errors for total mass of both sub-10 μm and sub-2.5 μm particles were between 26 and 32% at 14:30 on each of the two days. The 44-h average total mass predictions differed from the data by 44–50%, indicating that mass predictions in the afternoon were better compared to those at other times of day. Figures 1–7 show time-series plots of predicted vs observed total mass in both size regimes at several locations.

3.2. *Elemental carbon*

Figures 8–14 show time-series plots of elemental carbon predictions vs observations. Elemental carbon (EC) gross errors were 19–23% at 14:30 on the first day of simulation, but increased to 33–39% at 14:30 on the second day. The 44-h average EC error was 50–58%, with EC_{10} errors less than $EC_{2.5}$ errors. The time-series plots show that EC_{10} concentrations at some locations improved by the second day of simula-

tion (e.g. at Anaheim, Claremont), suggesting that large errors at some stations overwhelmed smaller errors at other stations. Elemental carbon concentrations in the model were directly affected by emissions, coagulation, deposition, and transport. Also, growth of secondary material onto elemental carbon-containing particles caused EC-containing particles to increase in size.

Significant uncertainty exists in the accuracy of the particulate emissions inventory. For example, the baseline particulate inventory summarized in Table 1 may be too high for elemental carbon and other species (G. Cass, personal communication). The positive overall normalized bias for elemental carbon shown in Table 3 appear to confirm that the baseline inventory may be too high. Table 4 shows results from a sensitivity test in which the baseline inventory was cut to one-third its original value. This table shows that, while elemental carbon gross errors did not change significantly when emissions were reduced by two-thirds, the normalized bias decreased significantly. A possible conclusion is that true elemental carbon emissions lie between baseline and the one-third inventory emissions.
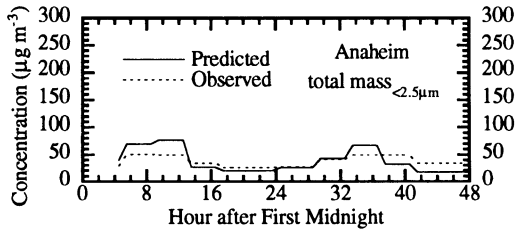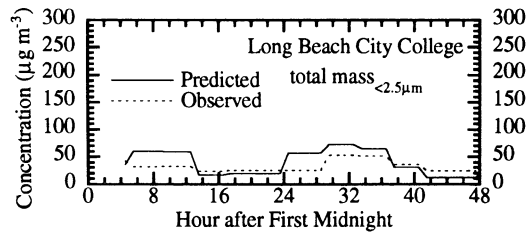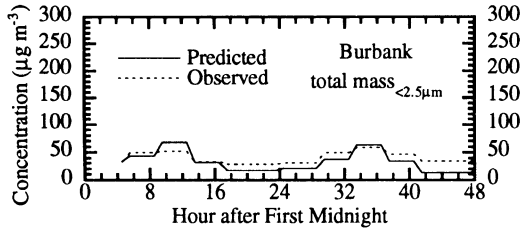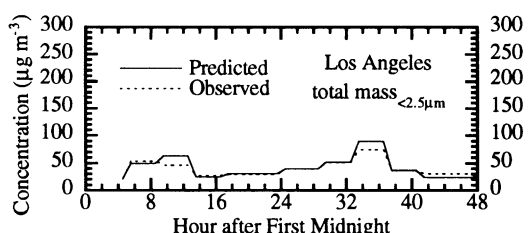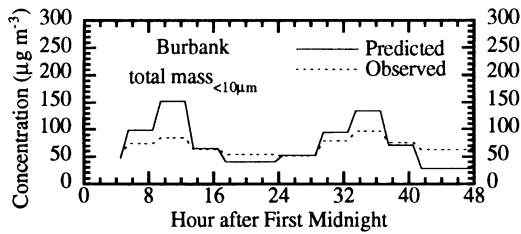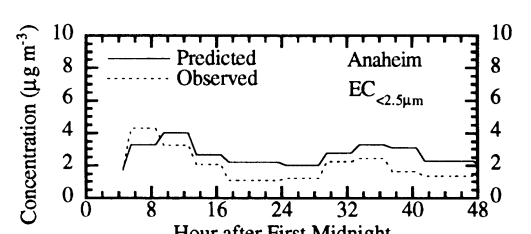
Fig. 1.

Fig. 2.

Fig. 3.

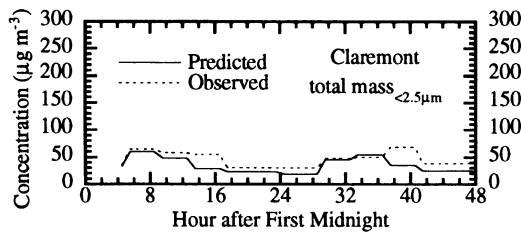Fig. 4.

Fig. 5.

Fig. 6.
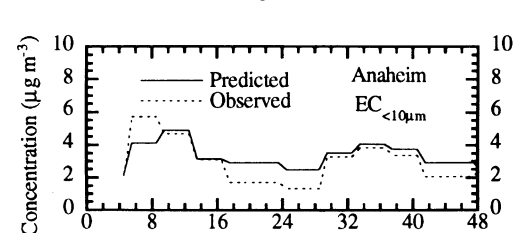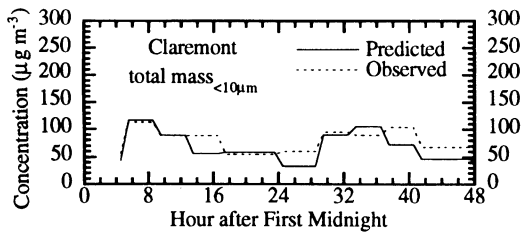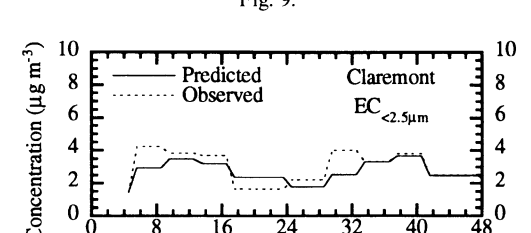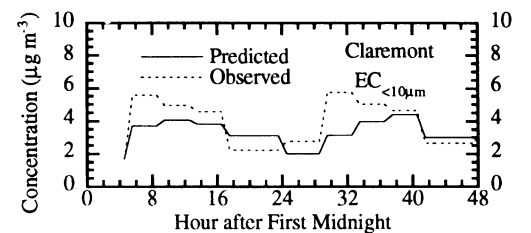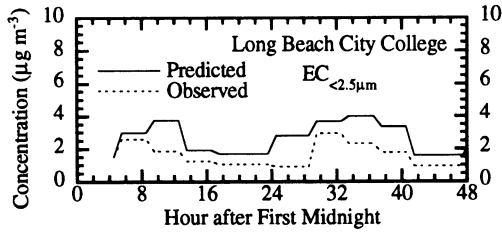

Fig. 7.
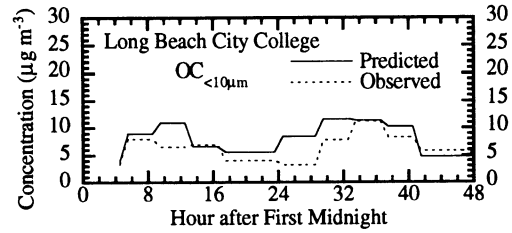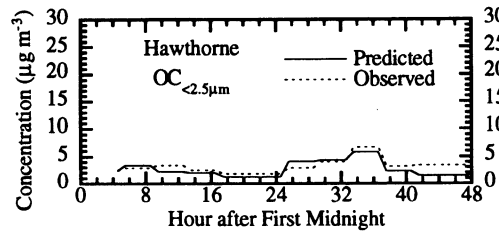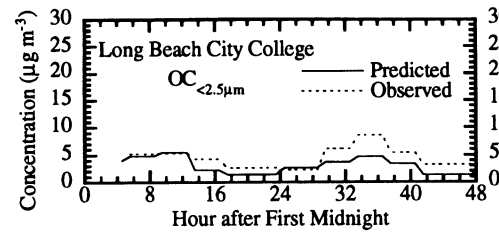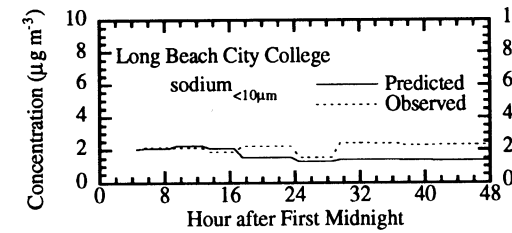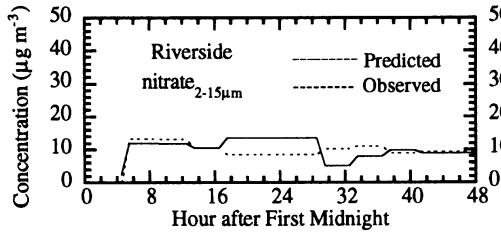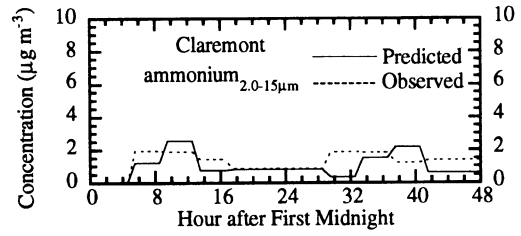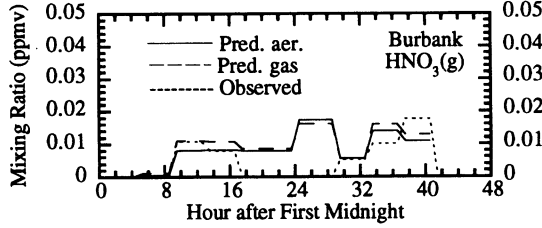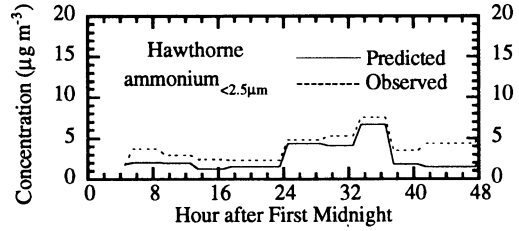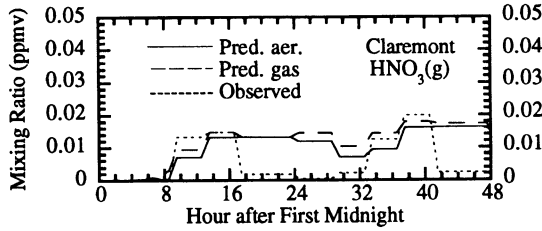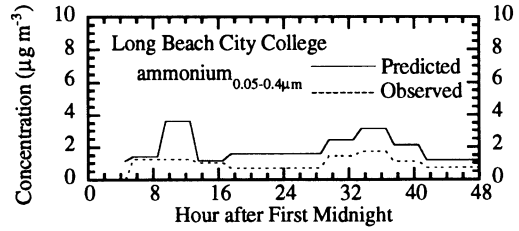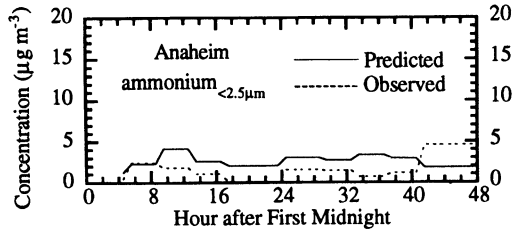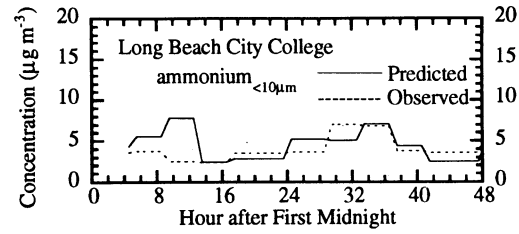

Fig. 8.

Fig. 9.

Fig. 10.

Fig. 11.

Figs 1–91. Time-series comparisons of base-case model results to data. Locations of the different stations are shown in Fig. 2 of Jacobson et al. (1996a). The time period for the simulation was 04:30 PST 27 August–0:30 PST 29 August 1987. In the case of particulate matter, observational data were often given as an average over a four-hour interval. Thus, model predictions were averaged over the same internal. In the plots with three curves, *Pred. aer.* is the predicted value curve with aerosol and gas processes turned on and *Pred. gas* is the predicted value curve with gas, but not aerosol processes turned on. In all cases where only two curves are shown, *Predicted* is the predicted value with both aerosol and gas processes turned on.

Fig. 12.
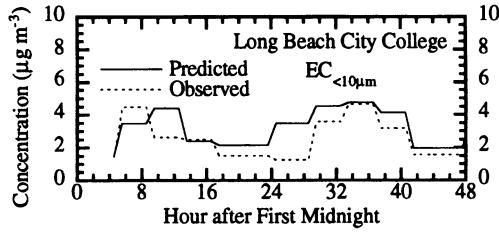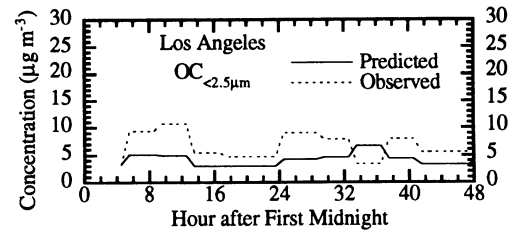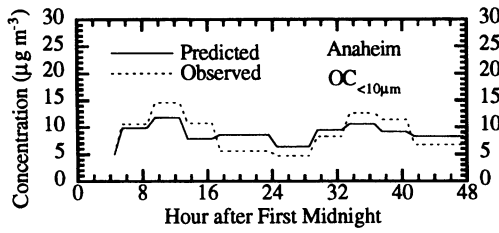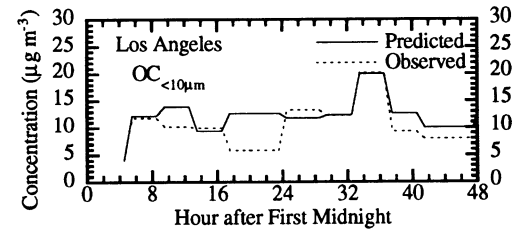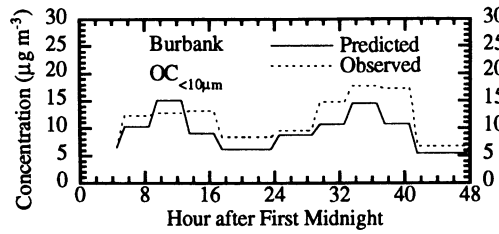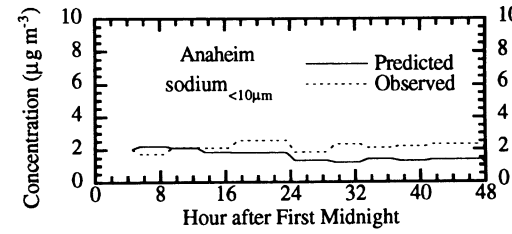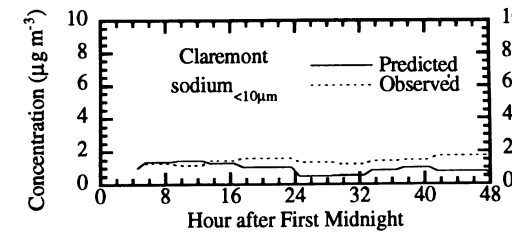
Fig. 13.

Fig. 14.

Fig. 15.

Fig. 16.

Fig. 17.

Fig. 18.

Fig. 19.

Fig. 20.

Fig. 21.

Fig. 22.

Fig. 23.

Fig. 24.

Fig. 25.

Fig. 26.

Fig. 27.

Fig. 28.

Fig. 29.

Fig. 30.

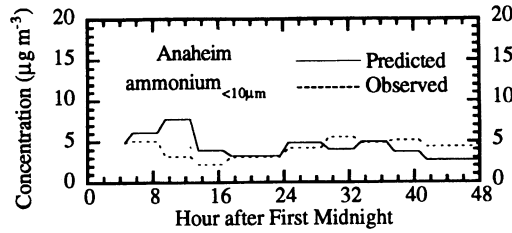Fig. 31.

Fig. 32.

Fig. 33.

Fig. 34.

Fig. 35.

Fig. 36.

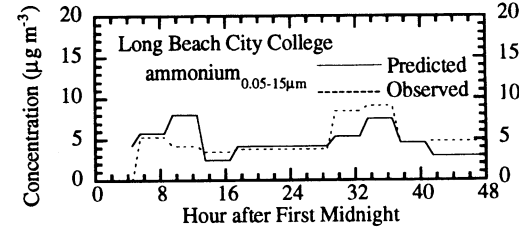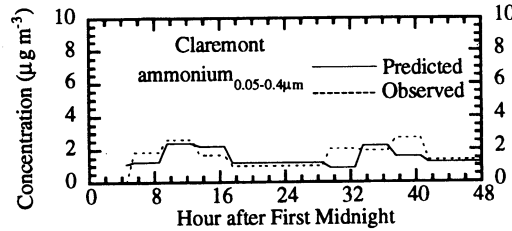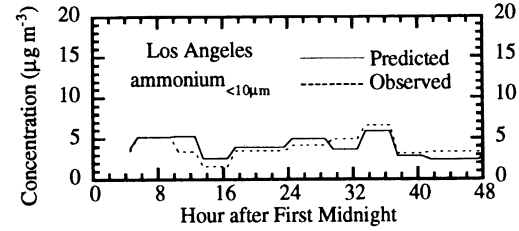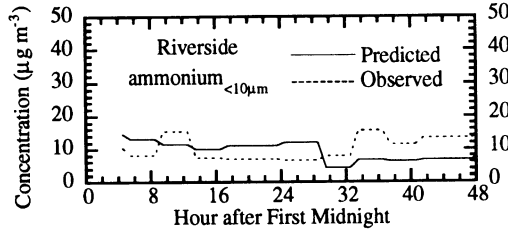Fig. 37.

Fig. 38.

Fig. 39.

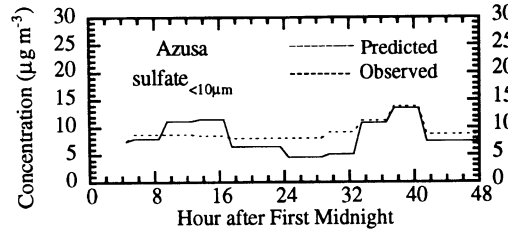Fig. 40.

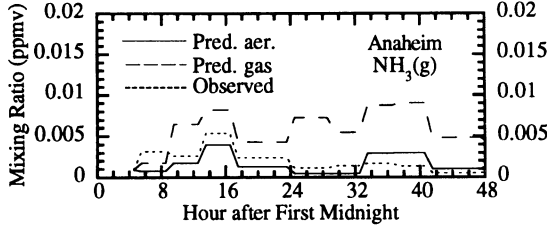Fig. 41.

Fig. 42.

Fig. 43.

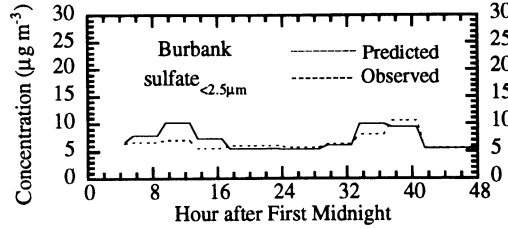Fig. 44.

Fig. 45.

Fig. 46.

Fig. 47.

Fig. 48.

Fig. 49.

Fig. 50.

Fig. 51.

Fig. 52.

Fig. 53.

Fig. 54.

Fig. 55.

Fig. 56.

Fig. 57.

Fig. 58.

Fig. 59.

Fig. 60.

Fig. 66.
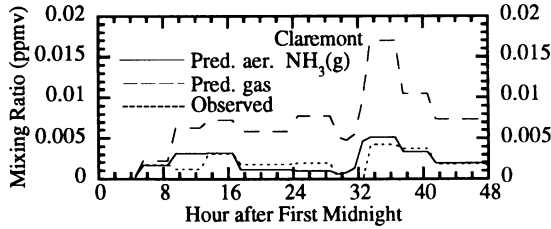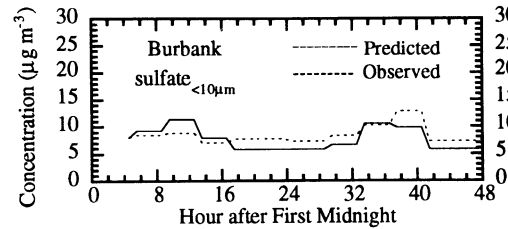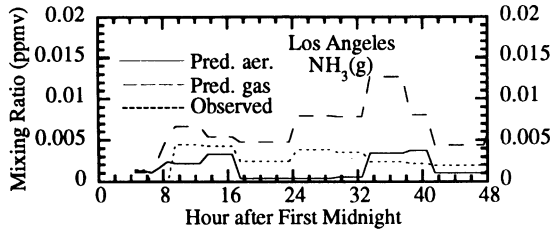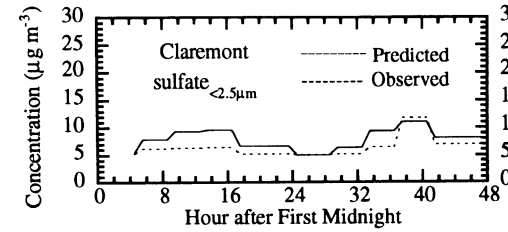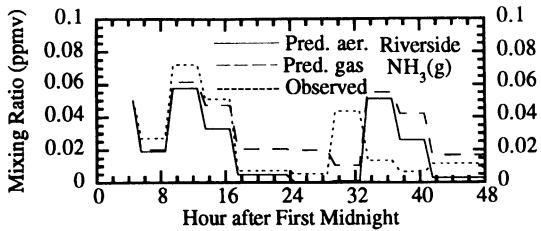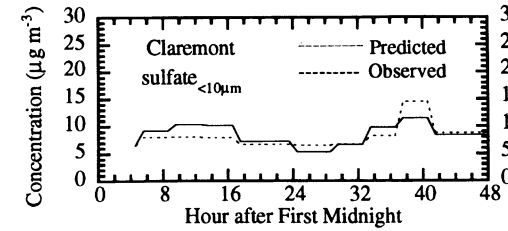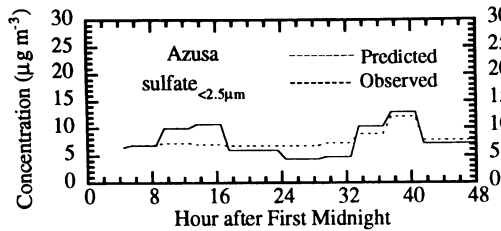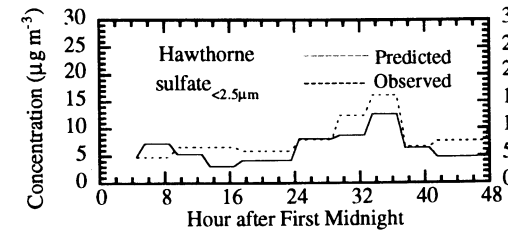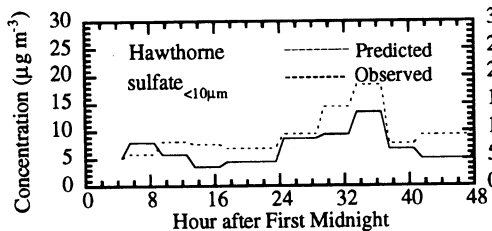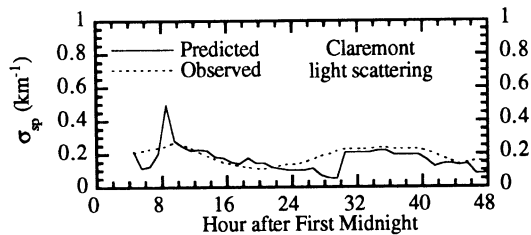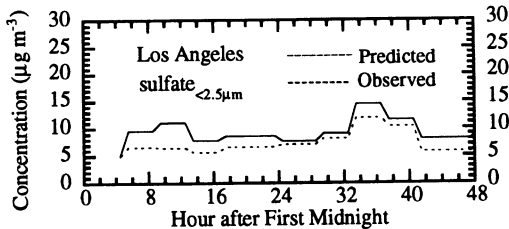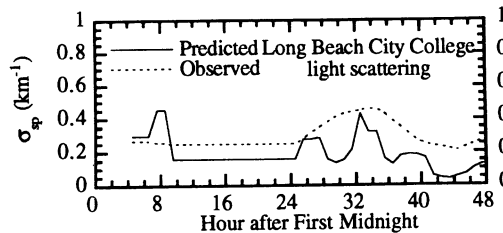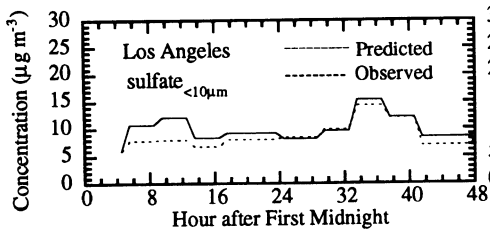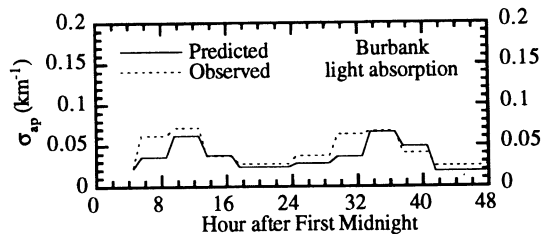

Fig. 61.

Fig. 67.

Fig. 62.

Fig. 68.
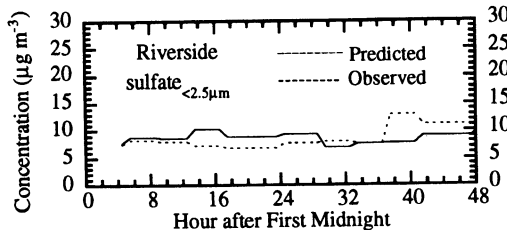
Fig. 63.
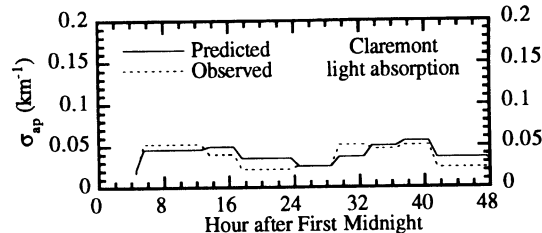
Fig. 69.
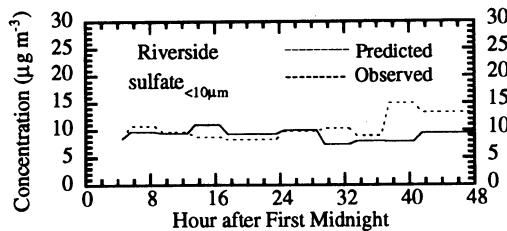
Fig. 64.
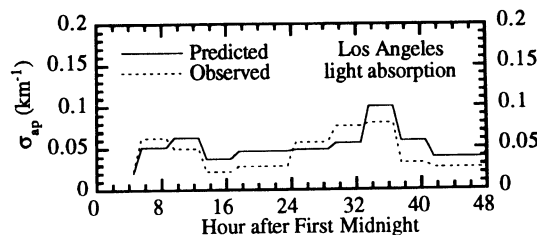
Fig. 70.
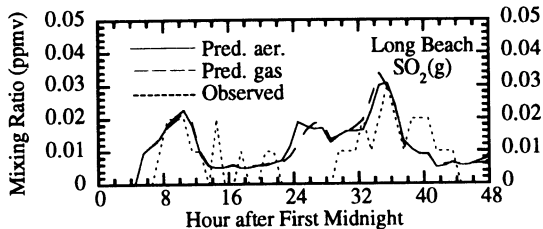
Fig. 65.
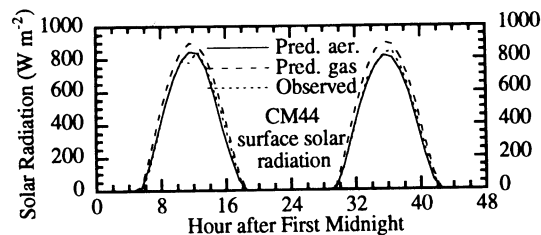
Fig. 71.
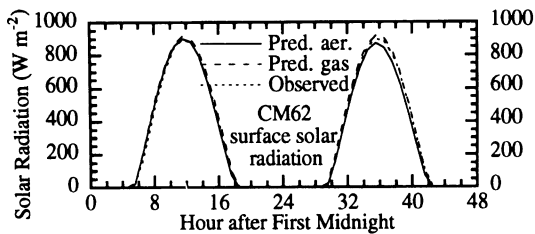
Fig. 72.
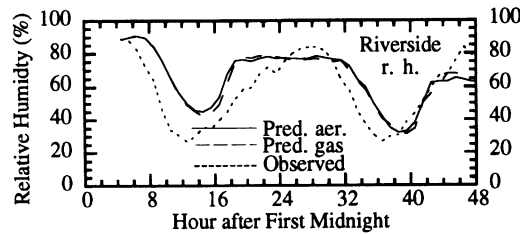
Fig. 73.
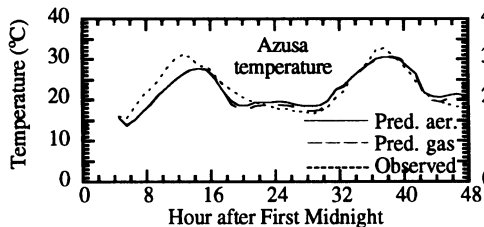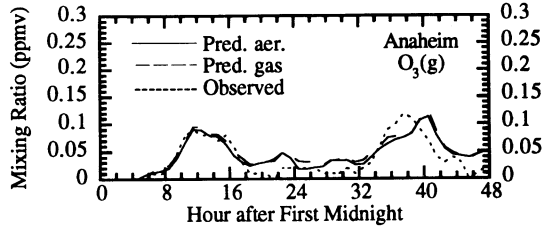
Fig. 74.

Fig. 75.

Fig. 76.

Fig. 77.

Fig. 78.

Fig. 79.
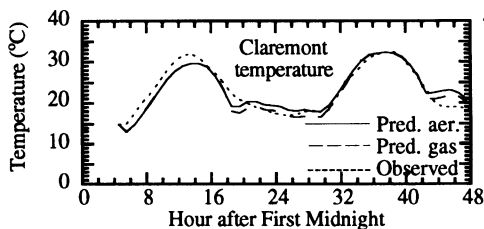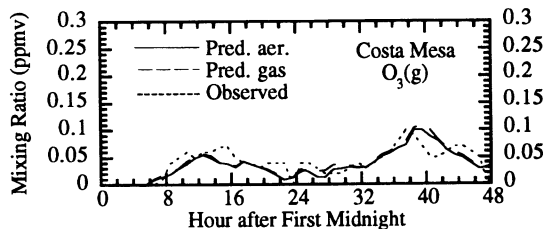
Fig. 80.
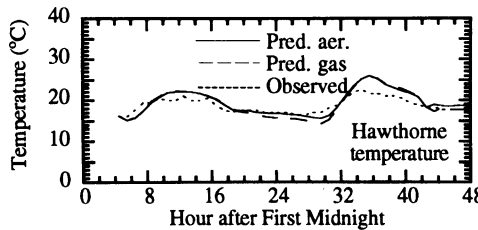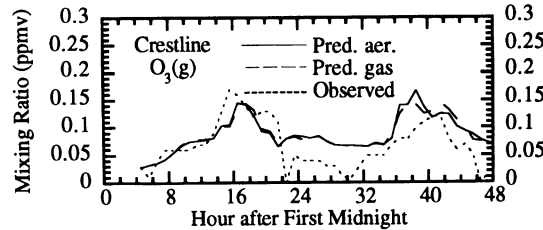
Fig. 81.
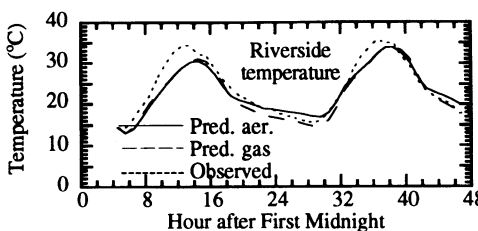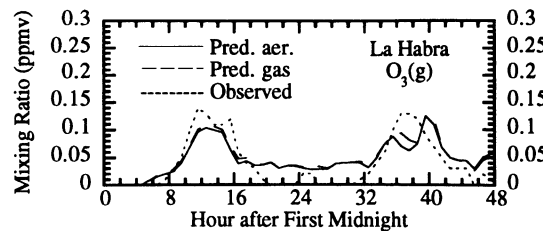
Fig. 82.
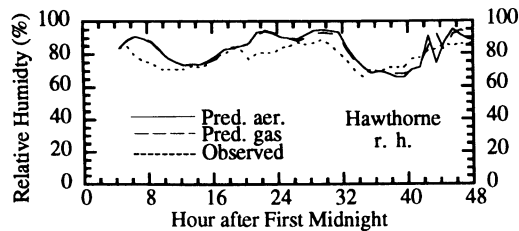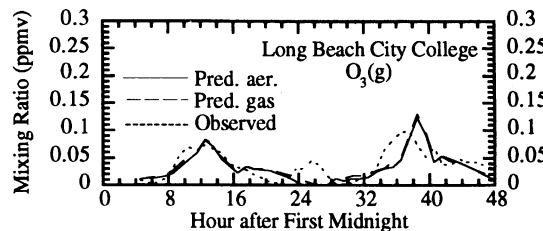
Fig. 83.
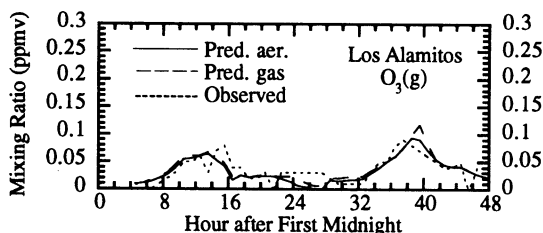
Fig. 84.
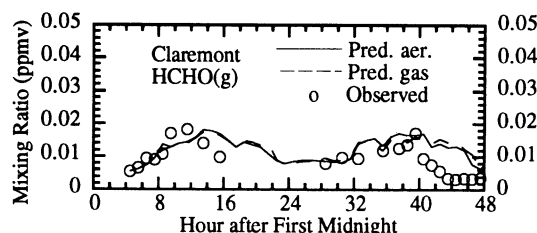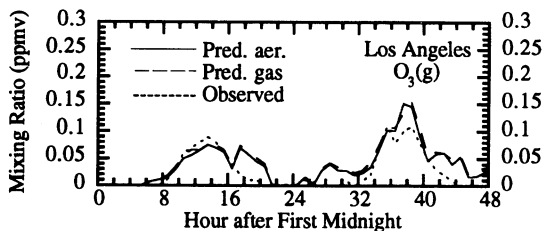
Fig. 85.
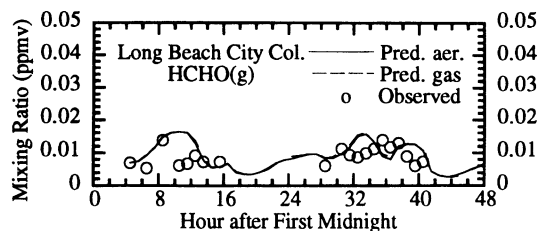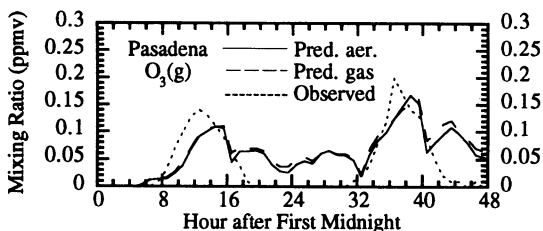
Fig. 86.

Fig. 87.

Fig. 88.

Fig. 89.

Fig. 90.

Fig. 91.
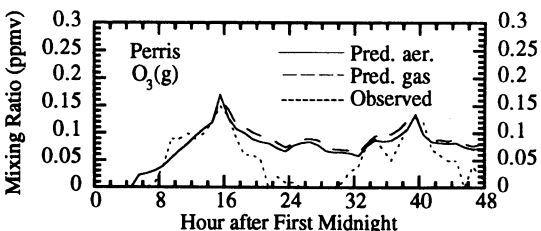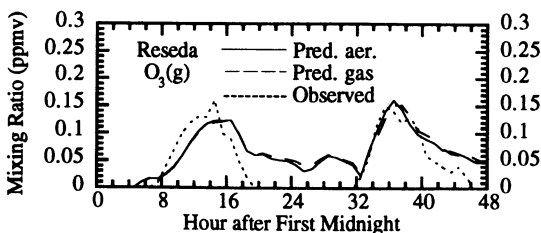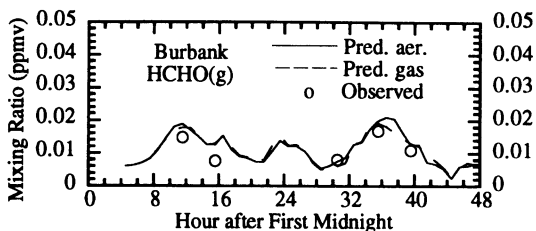
Nevertheless, time-series plots for elemental carbon and light absorption coefficient show good agreement with the data for the baseline inventory at several locations. Improvement in the accuracy of the baseline inventory for elemental carbon is expected to improve time-series comparisons of both elemental carbon and particle absorption.

3.3. Organic carbon

While the 44-h gross error for sub-2.5 μm organic carbon ($OC_{2.5}$) was less than that for $EC_{2.5}$, $OC_{2.5}$ predictions were biased much lower than were $EC_{2.5}$ predictions. This was expected since insufficient account was taken in the model of secondary organic particle formation. Secondary organic can comprise greater from 15–50% or more of total organic mass (Pandis et al., 1993). Further most of their contribution to total organic mass is in the submicron size range (Pandis et al., 1993), especially since growth does not significantly affect particles > 1 μm diameter (Whitby, 1978). For the simulations discussed here, organic gases were treated as condensable and/or soluble species. However, a significant number of additional condensable organic (e.g. Pandis et al., 1992) may need to be treated to account for the full difference between predicted and observed $OC_{2.5}$ concentrations. Thus, $OC_{2.5}$ underpredictions in the model were probably caused by insufficient treatment of condensable organics.

An alternative hypothesis is that OC emissions were underestimated. In fact, when all particulate emissions were doubled in a second sensitivity test (Table 4), the $OC_{2.5}$ gross error decreased from 49 to 40.1% and the bias decreased from − 44.1% to − 3.6%, indicating an improvement. However, the OC_{10} gross error simultaneously increased from 45.4 to 100.4% and the bias increased from 0.33 to 88.5%. Thus, the improvement in $OC_{2.5}$ due to increasing

Table 4. Gross errors and normalized biases, averaged over the entire 44-h model simulation, after five sensitivity simulations were run

Parameter	No. of comparisons	44-h average with one-third particles emissions		44-h average with double particle emission		44-h average with zero particle inflow at boundaries		44-h average with zero gas and particle initial values and inflow		44-h average starting meteorology 24 h in advance	
		Gross error (%)	Bias (%)	Gross error (%)	Bias (%)	Gross error (%)	Biass (%)	Gross error (%)	Bias (%)	Gross error (%)	Bias (%)
Mass$_{10}$	360	56.6	-48.8	99.1	82.6	49.7	1.4	44.9	-28.4	57.8	14.4
Mass$_{2.5}$	356	56.5	-51.8	71.1	48.3	43.7	49.7	47.1	-41.4	48.6	-6.7
EC$_{10}$	356	57.4	-53.1	132.6	121.8	50.1	15.3	54.3	5.7	70.9	31.9
EC$_{2.5}$	356	52.9	-47.6	158.0	149.2	57.4	29.6	61.3	20.2	75.3	43.8
OC$_{10}$	352	58.9	-57.9	100.4	88.5	44.8	-1.7	49.9	-12.6	55.9	11.7
OC$_{2.5}$	352	69.7	-69.4	40.1	-3.6	49.5	-44.4	60.7	-57.9	47.5	-41.5
Na$_{10}$	360	42.2	-38.3	31.6	-23.4	47.4	-41.5	88.9	-88.9	28.0	-25.1
NH$_4^+{}_{10}$	325	45.7	-4.7	47.6	5.5	49.5	-4.7	73.2	-72.3	42.8	-0.63
NH$_4^+{}_{2.5}$	321	57.1	-54.6	52.3	-47.2	57.2	-54.9	82.8	-82.8	54.2	-48.6
SO$_4^={}_{10}$	304	41.7	-40.4	50.8	39.9	27.3	-10.0	50.0	-49.2	30.1	-11.1
SO$_4^={}_{2.5}$	360	35.2	-32.2	65.4	58.3	28.9	2.0	44.2	-42.1	31.3	0.61
NO$_3^-{}_{10}$	360	68.5	11.0	77.7	30.1	69.9	17.4	69.7	-60.0	61.0	17.0
NO$_3^-{}_{2.5}$	360	67.9	-26.5	70.5	-8.6	69.1	-18.3	72.4	-62.9	68.1	-15.1
Cl$_{10}$	190	47.6	29.2	58.8	34.8	55.5	-12.3	92.6	-92.6	48.1	33.5
O$_3$(g)	571	29.2	-15.5	28.8	-7.3	27.5	-6.3	79.7	-79.7	32.7	-11.4
SO$_2$(g)	339	36.3	-25.6	35.4	-24.2	34.8	-23.5	65.3	-61.0	44.3	-41.8
NH$_3$(g)	269	66.7	-24.7	74.9	-20.5	70.5	-22.0	118.3	81.6	74.8	-25.8
NHO$_3$(g)	109	47.1	8.9	55.7	21.8	56.4	25.0	52.9	-51.1	49.9	-15.4
HCHO(g)	61	34.9	14.2	47.3	35.3	45.5	33.5	45.6	-32.1	38.5	-1.0
Temp.	628	0.65	0.17	0.65	0.09	0.65	0.12	0.64	0.05	0.68	-0.35
Rel. hum.	358	21.6	2.9	22.0	4.8	21.9	3.77	21.6	4.6	20.5	-5.5
Solar rad.	50	8.4	-0.81	14.4	-10.1	8.1	-3.1	8.8	2.6	12.2	-5.4
σ_{sp}	125	57.6	-48.0	61.3	36.8	43.2	-14.0	56.3	-52.0	45.9	-32.6
σ_{ap}	255	54.8	-59.0	133.9	124.8	40.3	16.0	42.5	-0.9	50.3	19.5

Note. Cutoff values are the same as those in Table 3.

emissions appears to have been for the wrong reason, and treatment of secondary gas-to-particle conversion of organic species should be improved in the model. Figures 14–20 show time-series comparisons of OC predictions to data.

3.4. Sodium

Sodium concentrations in the model depend significantly on sea spray and less on land-based emissions. Land-based emissions of sodium in August 1987, were estimated from the inventory as about 5 t per day. The primary sources were paved road dust and diesel emissions. On the other hand, sodium is one of the largest trace component of sea spray. Once emitted, sodium in the model was affected by transport, deposition, and growth of sodium-containing particles. Coagulation did not significantly affect the size-distribution of sodium-containing particles since sodium resides primarily in coarse-mode particles, which are not affected significantly by coagulation.

Model predictions of sodium concentrations were good. However such results were due to realistic initialization of sodium concentrations in the model. Figures 21–24 show that sodium concentrations were fairly constant during the simulation period, through both day and night. This factor indicates that initial concentrations must be distributed relatively uniformly in the vertical; otherwise, during the afternoon rise of the inversion base, sodium-free air from aloft would dilute concentrations near the surface. This factor was confirmed with a test simulation. During this simulation, sodium concentrations were initialized with a modestly decreasing gradient in the vertical (concentrations reduced to about one-half their surface values at 200 m in altitude). After noon on the first day of simulation, sodium concentrations were reduced by 50–70% near the surface, causing an overall gross error, after 44 h of 55%, with a bias of −55%. By initializing sodium concentrations with a nearly uniform vertical concentration in the boundary layer, results improved drastically, so that the gross error after 44 h fell to 36.0%, with a −30.2% bias (Table 3).

3.5. Chloride

Chloride, like sodium, is emitted primarily in sea spray and spume drops. However, while sodium's land-based sources totaled about $5 \, t \, d^{-1}$, those of chloride were estimated to be about $21.5 \, t \, d^{-1}$ in August, 1987 (Table 1). The primary sources of land-based chloride are forest burning, gasoline combustion, agricultural burning, fireplace burning, chemical manufacturing, and soil dust (CARB, 1988; Saxena et al., 1993). Gaseous hydrochloric acid is also emitted through coal combustion and waste incineration. In fact, 98% of anthropogenic HCl(g) emissions are generally from coal combustion (Saxena et al., 1993). Since HCl emissions are about 5% of SO$_2$ emissions in the U.S. (Saxena et al., 1993) and since coal combustion is not a major industry in the Los Angeles

Basin, gaseous hydrochloric acid emissions were ignored in the model.

Unlike sodium, chloride is volatile; consequently, accurate predictions of chloride concentrations depend on accurate predictions of both emission and volatilization rates of chloride. Figures 25–27 show time-series comparisons of sub-10 μm chloride (Cl$_{10}$) predictions to data. The figures show that the observed Cl$_{10}$ mass decreased significantly during the day. Because Cl$_{2.5}$ data from SCAQS show that relatively little chloride existed in sub-2.5 μm particles for the simulation period, most observed Cl$_{10}$ mass resided in particles between 2.5 and 10 μm in diameter. Chloride did not exist in smaller particles because of continuous presence of acids, particularly sulfuric acid, in these particles. However, chloride was present in coarse-mode particles during nighttime while it disappeared from these particles during the day. Part of the reason chloride disappeared from coarse-mode particles during the day was because these large particles acidified during the day.

Acidification was caused in part because relative humidity decreased as each day progressed, causing liquid water content to decrease. The decrease in liquid water content increased the concentration of other acids, particularly nitric acid. In a competition between nitric acid and hydrochloric acid, nitric acid forces hydrochloric acid to the gas phase. Upon initial observation of the effective Henry's constant of HCl, it is not obvious that HCl should be forced out of solution by the presence of nitric acid. In fact, at 298 K, the effective Henry's constant of hydrochloric acid is similar to that of nitric acid. For example, the equilibrium expressions for the two species can be written as

$$\frac{m_{H^+} m_{Cl^-} \gamma_{H^+, Cl^-}^2}{p_{HCl(g)}} = K_{eq} = 1.97 \times 10^6 \quad \text{at 298 K} \quad (1)$$

$$\frac{m_{H^+} m_{NO_3^-} \gamma_{H^+, NO_3^-}^2}{p_{HNO_3(g)}} = K_{eq} = 2.51 \times 10^6 \quad \text{at 298 K} \quad (2)$$

where m is molality, p is partial pressure, γ is the activity coefficient, and K_{eq} is the effective Henry's constant, taken here from Kim et al. (1993). However, a closer observation of the binary activity coefficient of dissolved hydrochloric acid indicates that the coefficient increases exponentially at high molalities whereas the activity coefficient of dissolved nitric acid remains moderately low at high molalities (e.g. Fig. 1 of Jacobson et al., 1996b). In a solution with multiple components, the activity coefficient used in equations (1) and (2) is not a binary activity coefficient but an effective activity coefficient determined from a mixing formula that depends on the binary activity coefficient of all possible cation and anion pairs in the mixture. Each binary activity coefficient used in the mixing formula is determined by assuming that the molality of the binary species results in the current ionic strength of the mixture. Consequently, when the ionic strength of a mixture is high, the binary activity

coefficient of dissolved HCl to be used in the mixing formula is large, and the mixing formula predicts a large mixed activity coefficient of dissolved HCl, forcing HCl towards the gas phase via equation (1).

In sum, as the ambient relative humidity decreased during the day, observed chloride appears to have been forced out of coarse-mode particles because of the presence of nitrate in such particles. Although coarse-particle nitrate concentrations generally peaked in early morning and decayed during the day due to decreased relative humidity and to increased vertical mixing, nitrate concentrations did not decrease so rapidly as did chloride concentrations. Thus, perturbations in relative humidity affected chloride faster than they affected nitrate.

In the model, chloride concentrations were often, but not always, predicted better during the night than during the day. Errors in predicting daytime coarse-mode chloride appear to be due to a combination of errors in nitrate and relative humidity predictions. Since nitrate concentrations were typically more than five times greater than chloride concentrations, small daytime underpredictions in nitrate may have, in some cases, caused relatively large errors in daytime chloride predictions. In other cases, the relative humidity was predicted to be too high during the day, allowing excess chloride mass to be retained within particles.

3.6. Nitrate and nitric acid

Like chloride, nitrate is a volatile species. However, its land-based emission rate is small (about $3.1 \, t \, d^{-1}$ from Table 1), and its sea spray emission rate is insignificant. Particulate nitrate forms almost entirely by dissolution or heterogeneous reaction of nitric acid gas. In the model, nitrate concentrations were underpredicted in sub-2.5 μm particles. Part of the reason for the underpredictions appears to be that ammonium was underpredicted in fine particles. Since sulfate often dominates fine-particle mass, additional cations are needed in these particles if nitrate is to dissolve. Sodium exists mostly in coarse particles and its concentrations are fairly low; thus, sodium is unlikely to balance nitrate concentrations in fine particles. Ammonium, on the other hand is volatile, and its gas-phase precursor, ammonia, can be present in high mixing ratios. Thus, ammonium is more likely to accompany nitrate onto fine particles than is sodium. Figures 28–38 show time-series comparisons of model predictions of nitrate to data.

Gas-phase nitric acid in the model was overpredicted. Nitric acid gas mixing ratios depend not only on the rate of nitric acid transfer to and from particles, but also on the gas-phase oxidation rate of nitrogen dioxide, the deposition rate of nitric acid, and on other vertical and horizontal transport processes. Additional statistics from the base case simulation indicates that the largest source of nitric acid gas was gas-phase chemical reactions. Of all the nitric acid gas produced by chemical reactions, about 15% depos-

ited directly to the ground and about 50% transferred to the aerosol phase. However, the fact that fine-particle nitrate predictions were too low and nitric acid gas predictions were too high indicates that, on average, fine particles in the model did not contain enough ammonium, as discussed above. The dearth of model ammonium decreased the rate of transfer of some nitrate to fine particles. Figures 37 and 38 show time-series plots of nitric acid gas predictions and data of Long Beach City College.

3.7. Ammonium and ammonia

Figures 39–48 and 49–52 show time-series plots of ammonium and ammonia gas predictions, respectively, versus observations. Both ammonium and ammonia gas concentrations were biased low in the model (Table 3). Ammonia gas mixing ratios depend significantly on emissions, gas-to-particle conversion, advection, and diffusion. However, gas-phase chemical reactions do not affect ammonia mixing ratios significantly. The ammonia gas emissions inventory used (Section 2.4) dates back to 1982; consequently, some discrepancies in the model may have been due to changes in emission sources since that time. On the other hand, the direct particulate ammonium emissions rate was only about $1.1 \, t \, d^{-1}$; thus, the particulate inventory did not affect model results significantly.

Finally, Figs 49–52 show that the inclusion of aerosols in the model caused gas-phase ammonia gross errors and mixing ratios to decrease. Table 5 shows that the inclusion of aerosols caused mixing ratios to decrease by 58.1%, resulting in better comparisons to data (as shown in the figures). The improvement in ammonia gas mixing ratio predictions was expected since aerosols are a significant sink for ammonia, a soluble gas.

3.8. Sulfate and sulfur dioxide

Sulfate in the atmosphere has several sources. The baseline particulate inventory suggests that, in August 1987, approximately 54 t sulfate d^{-1} were emitted from land-based sources, including cement production, aircraft jet fuel combustion, petroleum refining, and paved road dust. This number is most likely too large (G. Cass, personal communication). Sea spray also contributed to the atmospheric sulfate burden. In addition, approximately $100 \, t \, d^{-1}$ of sulfur dioxide gas were emitted into Los Angeles. Much sulfur dioxide ended up as sulfate via gas-to-particle conversion processes. In addition to being direct emitted, sulfate entered model particles primarily by condensational growth of sulfuric acid. As shown in Figs 53–64 and Table 3, model predictions of fine and coarse sulfate matched observations well at nearly all observation sites in the basin.

Sulfur dioxide mixing ratios in the model were generally predicted to be low, although relatively accurate in comparison to several other species. However, SO_2 observations had a resolution of only

Table 5. Comparision of predicted parameter values, averaged over entire grid domain, when aerosols were not and were included in the model simulations

Parameter	No. of value	Without aerosols	With aerosols	Percent change due to aerosols
Solar rad. (W m^{-2})	52	547.6	494.3	− 9.7
Peak solar rad (W m^{-2})	8	856.4	801.4	− 6.4
Daytime temp. (K)	252	300.649	300.571	− 0.0259
Midday temp. (K)	112	302.380	302.300	− 0.0265
Nighttime temp. (K)	378	291.350	292.119	+ 0.264
Overall temp. (K)	630	295.069	295.500	+ 0.146
Wind speed (m s^{-1})	1452	2.575	2.580	+ 0.194
O_3 (g) (ppmv)	1662	0.0650	0.0637	− 2.0
PAN (g)	313	0.00248	0.00225	− 9.3
HNO_3 (g)	360	0.0111	0.00897	− 19.2
NH_3 (g)	360	0.00903	0.00378	− 58.1
SO_2 (g)	1026	0.007115	0.007103	− 0.17
HCHO (g)	360	0.011026	0.01102	− 0.054

Note. Solar radiation was averaged over all daytime hours, peak solar radiation was averaged from 11:30–13:30 over both days, daytime temperatures were averaged from 08:30 to 17:30 over both days, midday temperatures were averaged from 11:30 to 15:30 over both days, and nighttime temperatures were averaged from 18:30 to 07:30 over both nights. All other parameters were averaged over all 44 h of the simulations.

0.01 ppmv, and typical mixing ratios at most locations were close to this value; consequently, gross errors in SO_2 mixing ratios were not the best indicator of performance. Time-series plots, such as that shown in Fig. 65, give a slightly better idea of performance in some cases.

Finally, Table 5 and Fig. 65 show that the inclusion of aerosols slightly decreased the ambient mixing ratio of sulfur dioxide gas. The primary reason the SO_2 mixing ratios did not decrease further was that little fog was predicted or observed during the simulation period. When aersols were included and the predicted relative humidity exceeded 100%, size resolved fog droplets were allowed to grow by condensation in the model. Because fog was relatively absent, little SO_2 could dissolve. However, the lack of predicted fog was consistent with the data. For example, during the simulation period, observed fog appeared after 10:30 p.m. on 28 August at the San Nicholas Island site (SNI), at 5:30 a.m. on 27 August and 12:30 a.m. on 29 August at the Simi Valley site (SIMI), and from 4.30–7.30 a.m. on 27 August and 12:30–8:30 a.m. on 28 August at the El Rio site (ELRI). Thus, fog appeared at only three locations, two of which (ELRI and SIMI) were relatively close to each other. The model predicted fog at Simi Valley at 5:30 a.m. on 27 August and 20 mile to the southeast of Simi Valley at 12:30 a.m. on 28 August (the last hour of simulation). Further, a fog was nearly predicted at SNI and ELRI at the remaining times that a fog was observed. In sum, the small decrease in sulfur dioxide mixing ratios that occurred when aerosol processes were included was expected since little fog was observed or predicted during the simulation period.

3.9. *Light scattering and absorption*

Two other indicators of aerosol module performance are the prediction of particle absorption coef-

ficient (σ_{ap}) and particle scattering coefficient (σ_{sp}). The particle absorption coefficient depends on the particle size distribution and the index of refraction of elemental carbon. The scattering coefficient also depends on size distribution and index of refraction. The method of calculating particle scattering and absorption efficiencies and corresponding extinction coefficients in the model was discussed in Jacobson (1996).

Figures 66 and 67, and 68–70 show time-series comparisons of light-scattering and absorption coefficients, respectively, to data for several locations. The 44-h gross errors were 43.0 and 39%, respectively. The accuracy of time-series plots for light absorption coefficient indicate that ambient elemental carbon predictions in the model were not far off at these locations.

In the model, one source of error with respect to the scattering coefficient was the fact that the predicted scattering coefficients were obtained at the ambient relative humidity while the observed coefficients were obtained with a heated inlet nephelometer (e.g. Eldering *et al.*, 1994); thus, the effective relative humidity of the observed distribution used for obtaining the observed scattering coefficient was often lower than that of the ambient distribution.

3.10. *Surface solar radiation*

Surface solar radiation predictions matched the data well. Normalized gross errors for the two sites measured were 4.3 and 6.3% at 14:30 PST on the first day and second days of simulation, respectively. Figures 71 and 72 show corresponding time-series plots. In these figures, solar radiation predictions are shown for both the base case and for the case without aerosols. Table 5 shows that the presence of aerosols decreased surface solar radiation by 6.4% (55 W m^{-2}) during peak daylight hours (11:30–13.30 each day) and by 9.7% during all daylight hours. The predicted decrease in surface solar radiation is consistent with

that measured by Peterson *et al.* (1978), who found a 6–8% decrease in solar radiation in Los Angeles in comparison to a non-urban region.

Of the two stations for which solar radiation data were compared, one (CM44) was near Riverside and the other (CM62) was near Temecula, in the south basin. Thus, radiation at the CM44 site was measured through a heavy aerosol loading while that at the CM62 site was measured through a slightly lighter loading. Figures 71 and 72 show that the inclusion of aerosol processes affected solar radiation at CM44 more than it did at CM62, which is expected, given the locations of the stations.

3.11. *Temperature and relative humidity*

Figures 73–75, and 76 and 77 show time-series comparisons of temperature and relative humidity predictions, respectively, to data. Table 3 shows that the gross error for temperature predictions was 0.63% (1.85 K), on average. Similarly, that for relative humidity predictions was 22% (14.0% r.h.). Table 5 shows results when the base-case simulation was run without the inclusion of aerosols. The table shows that daytime temperatures decreased by 0.0259% (0.078 K) whereas nighttime temperatures increased by 0.264% (0.77 K). Over both day and night, temperatures increased, on average, 0.146% (0.43 K). The increase in nightime temperatures is easily explained by the fact that aerosols increase the downward infrared flux of radiation to the surface, decreasing the nocturnal cooling rate of the surface (Zdunkowski *et al.*, 1976). A test case for the conditions at Claremont was performed to estimate the downward infrared flux and other parameters, during both day and night. Results are presented in Table 6. The table shows a predicted increase in nighttime downward infrared flux of 13 W m^{-2} due to the presence of aerosols. This number compares to a predicted increase of 15 W m^{-2} by Estournel *et al.* (1983) from a simulation of another case.

During the day, aerosols increase the downward infrared flux to the surface more than they do during the night. Table 6 shows an increase in daytime downward radiative flux of 19 W m^{-2} predicted by the present model. This compares to an increase of 22–25 W m^{-2} predicted by Estournell *et al.* (1983), The increase in downward infrared radiation increases heating rates at the bottom atmospheric layer. For the test case, the model predicted a shortwave daytime heating rate of + 0.52°C h^{-1} when aerosols were present at Claremont. This compare to 0.55°C h^{-1} given by Binenko and Harshvardhan (1993) for another location. When aerosols were absent, the model predicted a short wave daytime heating rate of + 0.25°C h^{-1}.

In sum, predicted air temperatures just above the surface increased during the night when aerosols were accounted for because they increased the downward flux of infrared radiation to the surface. As the sun rose in the morning, absorption and reemission by aerosols continued. However, during the day, aerosols attenuated direct solar radiation to the ground surface by about 6–10%, cooling the surface relative to the no-aerosol case. Although less solar radiation reached the surface during the day, the residual radiation was redistributed to other layers of the atmosphere by scattering and absorption/reemissions. Such redistribution prevented layers of air above the surface from cooling significantly. In fact, such layers warmed up, increasing the temperatures at the base and top of the inversion layer at each location. However, the reduction in surface radiation was sufficient to cause a net cooling of the bottom layer of air above the ground surface during the day. Since elevated layers warmed and the surface layer cooled, stability of the atmosphere increased and the inversion base height decreased slightly during the day due to the presence of aerosols.

Predicted temperatures just above the ground surface, averaged over day and night, were higher when aerosols were present compared to when they were not. Such net warming occurred because nighttime warming lasted for more hours and was stronger than daytime cooling.

Table 6. Comparison of values obtained from a test case to those obtained from other authors when a one-dimensional simulation was performed under conditions at Claremont

Parameter	Results from this work	Results from other authors
Change in surface solar radiation due to aerosols	− 58 W m^{-2} (− 6.5%)	− 6–8%*
Change in daytime downward IR flux to surface due to aerosols	+ 19 W m^{-2} (+ 21.8%)	+ 22–25 W m^{-2}†
Change in nighttime downward IR flux to surface due to aerosols	+ 13 W m^{-2} (+ 15.0%)	+ 15 W m^{-2}†
Daytime heating rate of bottom atmospheric layer in presence of aerosols	+ 0.52°C h^{-1}	+ 0.55°C h^{-1}‡

Note. Nighttime computational were performed for 04:30 and daytime computations were performed for 12:00. The calculations were instantaneous (not time dependent). Results from other authors were under different conditions. Thus, the comparisons provide only ballpark validation.
* Peterson *et al.* (1978).
† Estournel *et al.* (1982).
‡ Binenko and Harshvardhan (1993).

3.12. Ozone

Figures 79–88 show comparisons of predicted vs measured ozone mixing ratios, with and without the inclusion of aerosols. Table 5 shows that ozone mixing ratios decreased by about 2.0% when aerosols were included in the simulations. Aerosols affect ozone mixing ratios in at least three ways. First, they affect air temperatures, which affect chemical reaction rates, atmospheric stability, air pressure, and wind velocities. These parameters subsequently affect ozone mixing ratios. Second, aerosols remove some soluble organic gas precursors to ozone formation. However, aerosols do not significantly affect NO and NO$_2$ mixing ratios since these gases are relatively insoluble. Finally, aerosols affect ozone mixing ratios by directly attenuating solar radiation, which causes photodissociation rates to decrease. Since the model did not treat significant organic removal by aerosols, such removal was unlikely to be the major source of ozone reduction here. Also, the average temperature decrease of 0.43 K due to the presence of aerosols may be too small to cause ozone mixing ratios to decrease by 2%. On the other hand, the decrease in surface solar radiation by 6–10% appeared sufficient enough to have the greatest effect on the reduction in ozone mixing ratios.

3.13. Formaldehyde

An additional species compared was formaldehyde gas. Formaldehyde is not so soluble as HCl, HNO$_3$, or H$_2$SO$_4$; however, a fair fraction of it dissolves in fog-sized drops. Formaldehyde is emitted directly and undergoes chemical reactions with several species. Figures 89–91 show time series comparisons of predicted vs measured formaldehyde gas mixing ratio. The figures show predicted values, with and without the inclusion of aerosols in the model. The figures and corresponding statistics indicate that the predictions (with the inclusion of aerosols) were in good agreement with the data at Claremont and in fairly good agreement at Long Beach City College. Furthermore, for the given episode, aerosols did not absorb significant formaldehyde. This finding is expected for the same reason that aerosols did not absorb significant sulfur dioxide.

4. SENSITIVITY TESTS

In addition to the simulation without aerosols, five sensitivity cases were run. In the first, the CARB particulate emissions inventory was cut to one-third its original value. In the second, the particulate emissions inventory was doubled. In the third, aerosol concentrations entering the model domain from all lateral boundaries were set equal to zero. In the fourth, lateral and initial concentrations of both gases and aerosols were set to zero. In the last, meteorology

was started 24 h prior to the rest of the processes. Table 4 shows gross errors and biases, averaged over 44 h, for each of the sensitivity cases. These should be compared to base case results shown in the last two columns of Table 3.

First, cutting the particulate emissions inventory to one-third its original value increased gross errors but not significantly; however, it caused normalized biases to decrease significantly for many species. As mentioned in Section 3.2, baseline particulate emission estimates may be too high for many species. However, because the error in emissions for each species differs, a blanket reduction in all emissions by two-thirds probably does not adequately account for the errors in the inventory.

Second, doubling the particulate emissions inventory worsened results for every parameter except OC$_{2.5}$ and Na$_{10}$. However, as discussed in Section 3.3, the improvements in OC$_{2.5}$ prediction were misleading. Similarly, since original errors in sodium concentrations were probably due to underestimates in ocean, and not land based, emission rates, the improvements in Na$_{10}$ predictions resulting from this test were also misleading. Ocean emission rates were not doubled for this simulation.

Third, setting particulate concentrations outside the lateral boundaries to zero did not change results significantly for most species. For example, average changes were less than $\pm 1\%$ for most species. However, sodium and chloride prediction errors after 44 h increased from 36.0 to 47.4% and 46.8 to 55.5%, respectively, when lateral boundary conditions were set to zero. After the first 20 h, sodium prediction errors increased from 25.2 to only 26.3%; thus, boundary conditions did not affect results during the first day. Errors increased, however, during the second day. Thus, uncertainty in the boundary conditions affected results significantly over two days for those species with a high background concentration over the ocean.

Fourth, setting lateral and initial concentrations to zero for both gases and aerosols caused results to degrade for most parameters. For example, Table 4 shows that ozone mixing ratio gross errors increased by over 50 percentage points when this sensitivity test was run, indicating that ozone mixing ratios were strongly dependent on initial distributions, especially of reactive organic gases. In addition, fine sulfate prediction errors doubled, and errors for several other particulate components increased significantly. However, total mass and elemental carbon errors did not change significantly. In fact, Mass$_{10}$ concentrations improved slightly. However, in the base case, Mass$_{10}$ was overpredicted by 9.3% while in the sensitivity test, it was underpredicted by 28.4%. Similarly, elemental carbon biases decreased in the sensitivity test. Thus, the removal of lateral boundary and initial values turned overpredictions into underpredictions for some species, but caused severe degradation in prediction results for most. Consequently, initializing

concentrations with realistic values is important for improving model accuracy.

Finally, starting meteorology 24 h in advance worsened simulation results for most species. In order to perform this sensitivity test, radiation calculations from GATOR were decoupled from the MMTD for the first 24 h of simulation. During this time, radiation in the MMTD was calculated with its original parameterization. At 4:30 a.m. on the 27th, the rest of the model was activated and radiation from GATOR was recoupled to the MMTD. A comparison of results from Table 4 to those from Table 3 indicate that predictions of eight parameters (e.g. $OC_{2.5}$, Na_{10}, NH_{410}, $NH_{42.5}$, NO_{310}, $HNO_3(g)$, $HCHO(g)$, and relative humidity) improved when meteorology was started early, but those of the remaining 16 parameters in the table degraded. Consequently, *spinning up* the meteorological model did not improve results. In fact, it caused overall results to degrade in this case. Such a finding is expected since model errors accumulate and cannot un-accumulated over time.

5. COMPUTER TIMINGS

Simulations were run on both a Cray 90 and Cray J916 computer. The average speed of the program on a Cray 90 was 365 megaflops, and the average speed on the J916 was about one-fifth the speed on the Cray 90. A forty-four hour model simulation with aerosol processes required 23 h on the Cray 90. The corresponding time on a J916 was 115 h. Simulations on either computer required 52 megawords of central memory.

6. CONCLUSION

The GATOR/MMTD air pollution model was applied to the study of aerosol buildup in the Los Angeles Basin. Predictions of aerosol concentrations, gas mixing ratios, radiative parameters, temperature, and humidity were compared to data. Overall gross errors for sulfate, sodium, light absorption, temperature, surface solar radiation, sulfur dioxide gas, formaldehyde gas, and ozone were lowest among parameters compared (1–40%). Gross errors for elemental carbon, organic carbon, total particulate mass, ammonium, nitric acid gas, and light scattering, ammonia gas, and nitrate were larger.

Simulations were performed with and without aerosol processes included in the model. The presence of aerosols reduced peak daytime surface solar radiation by approximately 6.4% (55 W m^{-2}), increased nighttime surface air temperatures by about 0.77 K, decreased daytime temperatures by about 0.08 K, and increased overall temperatures (day plus night) by 0.43 K. The presence of aerosols also caused ozone mixing ratios to decrease by 2%.

Sensitivity analyses were run. Reducing the baseline particulate emissions inventory to one-third its original value increased underpredictions of many parameters without affecting gross errors significantly. Doubling the inventory cause gross errors of nearly all particulate species to escalate rapidly. Also, assuming aerosol concentrations outside the lateral boundaries were zero did not affect most species concentrations much after 44 h. However, sodium and chloride prediction accuracy decreased by 10% in this case. Further, setting gas and aerosol initial and boundary concentrations to zero caused severe degradation of results. Finally, *spinning up* the meteorological model 24 h in advance provided no advantage and, in fact, decreased prediction accuracy for most species.

REFERENCES

Allen P. and Wagner K. (1992) 1987 California Air Resources Board emissions inventory, magnetic tape numbers ARA806 and ARA807.

Andreas E. L. (1992) Sea spray and the turbulent air-sea heat fluxes. *J. geophys. Res.* **97**, 11,429–11,441

Bineko V. I. and Harshvardhan H. (1993) Aerosol effects in radiation transfer. In *Aerosol Effects on Climate* (edited by Jennings S. G.), pp. 190–232.

California Air Resources Board (CARB) (1988) Method used to develop a size-segregated particulate matter inventory. Technical Support Division, Emission Inventory Branch, California Air Resources Board, Sacramento, California.

Cass G. R., Gharib S., Peterson M. and Tilden J. W. (1982) The origin of ammonia emissions to the atmosphere in an urban area. Open File Report 82-6, Environmental Quality Laboratory, California Institute of Technology, Pasadena, California.

DaMassa J., Allen P., McGuire T., McNerny D., Ranzieri A. and Wagner K. (1992) Technical Guidance Document: Photochemical Modeling. California Environmental Protection Agency/Air Resources Board.

Eldering A., Cass G. and Moon K. C. (1994) An air monitoring network using continuous particles size distribution monitors: connecting pollution properties to visibility via Mie scattering calculations. *Atmospheric Environment* **28**, 2733–2749.

Estournel C., Vehil R., Guedalia D., Fontan J. and Druilhet A. (1983) Observations and modeling of downward radiative fluxes (solar and infrared) in urban/rural areas. *J. Clim. appl. Met.* **22**, 134–142.

Fitz D., Chan M., Cass G., Lawson D. and Ashbaugh L. (1989) A multi-component size-classifying aerosol and gas sampler for ambient air monitoring. Air and Waste Management Association paper 89–140.1.

Gharib S. and Cass G. R. (1984) Ammonia emissions in the South Coast Air Basin 1982. Open File Report 84-2, Environmental Quality Laboratory, California Institute of Technology, Pasadena, California.

Jacobson M. Z. (1994) Developing, coupling, and applying a gas, aersol, transport, and radiation model to study urban and regional air pollution. Ph.D. thesis, Department of Atmospheric Sciences, University of California, Los Angeles.

Jacobson M. Z. (1996) Development and application of a new air pollution modeling system. Part II: aerosol-module structure and design. Atmospheric Environment Part A, in review.

Jacobson M. Z., Lu R., Turco R. P. and Toon O. B. (1996a) Development and application of a new air pollution modeling system. Part I: gas-phase simulations. Atmospheric Environment 30B, 1939–1963.

Jacobson M. Z., Tabazadeh A. and Turco R. P. (1996b) Simulating equilibrium within aerosols and non-equilibrium between gases and aerosols. J. geophys. Res. 101, 9079–9091.

John W., Wall S. M., Ondo J. L. and Winklmayr W. (1989) Acidic aerosol size distributions during SCAQS. Final Report for the California Air Resources Board under Contract No. A6-112-32.

Kim Y. P., Seinfeld J. H. and Saxena P. (1993) Atmospheric gas-aerosol equilibrium I. Thermodynamic model. Aerosol Sci. Technol. 19, 157–181.

King D., Wheeler N. and Wagner K. (1990) Southern California Air Quality Study Modeling Date Archive. California Air Resources Board Technical Support Division, Sacramento, California.

Lawson D. R. (1990) The Southern California air quality study. J. Air Waste Man. Assoc. 40, 156–165.

Lide D. R. (ed.-in-chief) (1993) CRC Handbook of Chemistry and Physics. CRC Press, Boca Raton, Florida.

Lu R. and Turco R. P. (1995) Air pollutant transport in a coastal environment Part II: Three dimensional simulations over the Los Angeles Basin. Atmospheric Environment 29, 1499–1518.

Lu R., Turco R. P. and Jacobson M. Z. (1996) An integrated air pollution modeling system for urban and regional scales. Part I: structure and Performance. J. geophys. Res. (in press).

Monahan E. C., Fairall C. W., Davidson K. L. and Boyle P. J. (1983) Observed interrelations between 10 m winds, ocean whitecaps and marine aerosols. Q. Jl. R. Met. Soc. 109, 379–392.

Monahan E. C., Fairall C. W. and Davidson K. L. (1986) A model of marine aerosol generation via whitecaps and wave disruption. In Oceanic Whitecaps and their Role in Air-Sea Exchange Processes (edited by Monahan E. C. and MacNiocaill G), pp. 167–174. D. Reidel, Norwell, Massachusetts.

Pandis S. N., Harley R. A., Cass G. R. and Seinfeld J. H. (1992) Secondary organic aerosol formation and transport. Atmospheric Environment Part A 26, 2269–2282.

Pandis S. N., Wexler A. S. and Seinfeld J. H. (1993) Secondary organic aerosol formation and transport — II. Predicting the ambient secondary organic aerosol size distribution. Atmospheric Environment Part A 27, 2403–2416.

Peterson J. T., Flowers E. C. and Rudisill J. H. (1978) Urban-rural solar radiation and atmospheric turbidity measurements in the Los Angeles Basin. J. appl. Met. 17, 1595–1609.

Pilinis C., Seinfeld J. H. and Seigneur C. (1987) Mathematical modeling of the dynamics of multicomponent atmospheric aerosols. Atmospheric Environment 21, 943–955.

Pilinis C., Seinfeld J. H. and Grosjean D. (1989) Water content of atmospheric aerosols. Atmospheric Environment 23, 1601–1606.

Russel A. G. and Cass G. R. (1986) Verification of a mathematical model for aerosol nitrate and nitric acid formation and its use for control measure evaluation. Atmospheric Environment 20, 2011–2025.

Saxena P., Mueller P. K. and Hildemann L. M. (1993) Sources and chemistry of chloride in the troposphere: a review. In Managing Hazardous Air Pollutants: State of the Art (edited by Chow W. and Connor K. K.). Lewis, Boca Raton.

Tesche T. W. (1988) Accuracy of ozone air quality model. J. Environ. Eng. 114 (4), 739–752.

Venkataraman C. and Friedlander S. K. (1994) Size distributions of polycyclic aromatic hydrocarbons and elemental carbon. 2. Ambient measurements and effects of atmospheric processes. Envir. Sci. Technol. 28, 563–572.

Welch R. and Zdunkowski W. (1976) A radiation model of the polluted atmospheric boundary layer. J. atmos Sci. 33, 2170–2184.

Winer A. M., Beiermann H. W., Dinoff T., Parker L. and Poe M. P. (1989) Measurements of nitrous acid, nitrate radicals, formaldehyde and nitrogen dioxide for the SCAQS by differential Optical Absorption Spectroscopy. Statewide Air Pollution Research Center, University of California, Riverside, California. Report to the California Air Resources Board under Contract A6-146-32.

Whitby K. T. (1978) The physical characteristics of sulfur aerosols. Atmospheric Environment 12, 135–159.

Woodcock A. H. (1953) Salt nuclei in marine air as a function of altitude and wind force. J. Meterol. 10, 362.

Wu J. (1993) Production of spume drops by the wind tearing of wave crests: the search for quantification. J. geophys. Res. 98, 18,221–18,227.

Zdunkowski W. G., Welch R. M. and Paegle J. (1976) One dimensional numerical simulation of the effects of air pollution on the planetary boundary layer. J. atmos. Sci. 33, 2399–2414.